APPLICATION OF COARSE INTEGRATION TO BACTERIAL CHEMOTAXIS*

S. SETAYESHGAR†, C. W. GEAR‡, H. G. OTHMER§, AND I. G. KEVREKIDIS¶

Abstract. We have developed and implemented a numerical evolution scheme for a class of stochastic problems in which the temporal evolution occurs on widely separated time scales and for which the slow evolution can be described in terms of a small number of moments of an underlying probability distribution. We demonstrate this method via a numerical simulation of chemotaxis in a population of motile, independent bacteria swimming in a prescribed gradient of a chemoattractant. The microscopic stochastic model, which is simulated using a Monte Carlo method, uses a simplified deterministic model for excitation/adaptation in signal transduction, coupled with a realistic, stochastic description of the flagellar motor. We show that projective time integration of "coarse" variables can be carried out on time scales long compared to those of microscopic dynamics. Our coarse description is based on the spatial cell density distribution. Thus we are assuming that the system "closes" on this variable so that it can be described on long time scales solely by the spatial cell density. Computationally, the variables are the components of the density distribution expressed in terms of a few basis functions, given by the singular vectors of the spatial density distribution obtained from a sample Monte Carlo time evolution of the system. We present numerical results and analysis of errors in support of the efficacy of this time-integration scheme.

1. Introduction. A recurring bottleneck in computational modeling of physical processes is the existence of multiple space and/or time scales. Important examples include patterns in fluids, defect dynamics in solids, and molecular dynamics of macromolecules. For example, in the latter case, the evolution of the physical configuration from initial to final state typically occurs on the time scale of milliseconds, while the interactions between constituent components must be resolved on the picosecond time scale. Furthermore, it is increasingly important in simulating biological systems to have a hybrid computational framework for interacting stochastic and deterministic processes, which occur on different time scales. Multiscale computational methods combine processing on fine space/time scales according to the governing microscopic description with macroscopic changes on a coarse grid (see, for example, [1, 2, 3]).

Here we present a computational scheme for "coarse projective" time integration of the macroscropic dynamics of stochastic processes that involve multiple, widely separated time scales. To illustrate the method we apply it to a microscopic model that

---

generates the biased random walk describing the macroscopic motion of a bacterium such as *E. coli* in an attractant gradient. The microscopic model, which will be described in detail in section 3.1, is a detailed model for the stochastic behavior of each bacterium that determines its position in space as a function of time. At the macroscopic level we are interested in the slow dynamics of physical quantities such as the density of the bacteria in space, so we wish to carry at the coarse level only sufficient information to determine those slow dynamics. (It will be seen that, in this problem, the density of bacteria is sufficient.) The methods we use will extract low-dimensional approximations to the bacterial density and its time derivatives from short bursts of microscopic simulation, permitting the *coarse integration* in time of the density. The focus of our analysis in this paper is the computational scheme, and, as such, our results address its plausibility rather than the phenomenology of chemotaxis.

In section 2 we discuss previous work on coarse time integration of microscopic dynamics and the new features of the method developed here, and we motivate its application to chemotaxis. The phenomenology of chemotaxis, the microscopic model of this process adopted in this work, and the corresponding Monte Carlo (MC) implementation of it are presented in section 3. We outline the coarse integration scheme in section 4 and present numerical results and analysis of errors in section 5. We conclude with future extensions and applications of this work.

2. Previous work. The traditional approach to studying long-term dynamics of multiscale processes involves (a) the derivation of a "coarse-grained" set of evolution equations, followed by (b) the analytical and/or computational study of these reduced equations using established, continuum numerical analysis tools. Recently, a so-called "equation-free" approach to the study of the coarse-grained behavior of such problems has been proposed which circumvents the first step [4, 5, 6]. This computational approach is based on the "coarse" or macroscopic time-stepper, a map from the coarse variables at time $t = 0$ to those at time $t = T$, where T is typically much larger than characteristic microscopic time scales in the system. This map is not obtained directly from the macroscopic evolution equations, which we may not know, but rather through short time evolution intervals of appropriately initialized microscopic simulations. The initial macroscopic variables are *lifted* to microscopic variables to initialize the microscopic simulation. At the completion of a burst of microscopic simulation, the microscopic variables are *restricted* back to macroscopic variables, providing an approximation to the macroscopic time step. This provides a *chord* of the macroscopic solution, which is an approximation to the time derivative of the macroscopic solution. This value can then be used in any conventional continuum numerical method for the macroscopic equations. This approach has been applied in several microscopic contexts, and the results appear to be promising [7, 8, 9, 10].

In this work we apply the coarse time-stepper in a projective integration study of a spatially distributed kinetic Monte Carlo simulation of a biased random walk. When, as in this case, the microscopic equations are stochastic, an effective algorithm must reduce the variance inherent in individual realizations of the stochastic process to a level that can be tolerated by the continuum numerical algorithm applied to the coarse system. This can be done by lifting to multiple copies or, as is done here, by estimating the derivative from a least squares fit to a large number of microscopic time steps. The projective integration method applied here uses a derivative estimate for the projective step, so that the stochastic noise is amplified by the reciprocal of the effective step length used in the derivative estimate. Hence, variance reduction is

very important. Augmenting the number of copies of the simulation (which, for our noninteracting particle model, corresponds also to a simulation with a larger number of cells) is the most direct approach to variance reduction; other variance reduction schemes are discussed in [11, 12].

In the context of bacterial chemotaxis, the computational scheme developed here can be viewed as a direct method to compute the macroscopic evolution of the cell density in space and time without actually deriving these equations. An alternate approach begins with the transport equation for the velocity-jump process, in which discontinuous changes in the direction (or speed) of an individual cell are generated by a Poisson process. It can be shown rigorously that this reduces to the chemotaxis equation under suitable scaling of space and time [13]:

$$(2.1) \qquad \frac{\partial \mu_0}{\partial t} = \vec{\nabla} \cdot \left(D \vec{\nabla} \mu_0 - \mu_0 \chi(S) \vec{\nabla} S \right).$$

In the above, $\mu_0(\vec{r}, t)$ represents the density of particles at spatial position $\vec{r}$ at time t, D is the diffusion constant, S is the concentration of the chemotactic attractant/repellent, and $\chi(S)$ is the chemotactic sensitivity. In general, it is difficult to explicitly determine the diffusion constant and chemotactic sensitivity when dependence on cell internal state variables is included in the transport equation, although work since completion of this paper addresses some of these issues [14, 15].

In section 3.1, we present a discrete (individual cell-level, rather than cell density-level) model of chemotaxis that combines a continuous, idealized model of signal transduction with a stochastic, two-state model of the motor response ("inner solver"). Work on obtaining macroscopic equations from such a microscopic model is in progress. However, the main contribution of the work presented here is to show how a macroscopic time-stepper ("outer solver") can be used in the time evolution of the spatial density, even though the macroscopic evolution equations are not known or may not be easily derived. This work extends previous coarse projective integration approaches in several respects: (i) it is the first use of dynamic, proper orthogonal decomposition basis functions as the appropriate macroscopic variables; (ii) it is the first application of combining a "hybrid" kinetic Monte Carlo and continuum, ordinary differential equation "inner solver" with a projective integration "outer solver"; and (iii) it is the first attempt at coarse integration of a biased random walk problem for which the unknown, effective macroscopic equations include spatially varying coefficients, due to the presence of an external chemoattractant potential.

3. Bacterial chemotaxis. The ability to sense and respond to environmental cues is necessary for the survival of most organisms. *E. coli* is a common and well-known single cell organism, with roughly 4000 genes, whose chemotaxis network has emerged as a prototype for understanding signal transduction networks in general [16, 17, 18, 19, 20]. Its genome is known, the crystal structures of many proteins have been obtained, and a large number of mutant strains exist, allowing detailed behavioral studies.

For each cell, chemotactic behavior begins when attractant or repellent molecules bind to membrane receptors, triggering a cascade of chemical reactions inside the cell that culminates in the production of the phosphorylated form of a response regulator protein (CheY-P) which controls the direction of rotation of the flagellar motor. The series of reactions that converts the extracellular signal (attractant/repellent) into cellular response is referred to as the signal transduction pathway. Flagella possess an inherent chirality, such that counterclockwise (CCW) rotation results in the bundling

up of the four to six flagella per cell, allowing them to act as a single propeller and leading to smooth swimming motion of the bacterium. When the flagella rotate clockwise (CW), the bundle flies apart and the bacterium tumbles. As conditions become increasingly favorable due to increase in chemoattractant concentration, a bacterium extends its run length; otherwise, it tumbles, and the subsequent direction of motion is randomly chosen, allowing a more favorable direction to be discovered. The resulting motion is a biased random walk toward favorable conditions and away from less favorable ones.

The sequence of biochemical reactions that take place inside a bacterium, starting with the binding of an attractant or repellent molecule to receptors on the cell surface and leading to the change in concentration of the response regulator species, CheY-P, has been extensively studied. Both deterministic models of these biochemical pathways, based on the law of mass action and Michaelis–Menten kinetics [21, 22], as well as fully stochastic models, exist [23]. The resulting measurement of the change in concentration of external signaling molecules by the cell is achieved through a temporal rather than a spatial comparison: fast sampling of the present external concentration is compared with the memory of that concentration some time ago. Order-of-magnitude analyses for why measurement of concentration changes across the cell length is not physically feasible have been given [24].

Memory in the signal transduction network is achieved through the existence of fast and slow reaction time scales. The fast reactions are receptor-ligand binding and phosphorylation kinetics; the slow reactions are methylation and demethylation. Ligand binding reduces the autophosphorylation rate of the corresponding membrane-bound receptor, in turn decreasing the rate of transfer of phosphoryl groups to CheY, and resulting in a (fast) drop in [CheY-P]. Addition of methyl groups to ligand-bound receptors restores the autophosphorylation rate, resulting in (slow) increase in [CheY-P]. The rate of demethylation becomes significant once a high methylation level is achieved. Hence, [CheY-P] reflects the balance between the fraction of ligand-bound receptors and methylated receptors. Perfect adaptation refers to the return of [CheY-P] to the same steady state level, regardless of the constant concentration level of the external stimulus. This value falls within the fixed operational range of the response of the flagellar motor to CheY-P.

The rotational bias of a single flagellum as a function of [CheY-P] has recently been accurately measured [25]. Interactions between flagella in the CW and CCW rotational states, which lead to the formation of flagellar bundles and ultimately determine whether the cell runs or tumbles, are the subject of current active research [26].

3.1. Microscopic model. In the model elaborated in this section, each bacterium is stationary or moving at a fixed speed. In this work, space is one-dimensional, so the velocity takes on one of two directions, left or right. Each bacterium has an internal state vector consisting of two continuum and six stochastic binary variables. The binary variables determine whether the bacterium is moving or not in a manner to be described below. The coupled, continuum variables, in effect, provide approximations to the concentration level of chemoattractant that the bacterium has recently encountered. The separation of "fast" and "slow" time scales for the dynamics of the continuous variables allows comparison of the chemoattractant levels at two different times, effectively enabling the bacterium to sense the spatial gradient of the chemoattractant along its path. This gradient estimate affects the probability that the bacterium will stop moving: the probability to stop and randomly select a new direc-

tion of motion decreases as the chemoattractant level increases. The resulting motion of a bacterium is a random walk, biased towards increasing attractant concentrations (and decreasing repellent concentrations).

In complex models, such as the one described in the subsections below, it is difficult to determine the Fokker–Planck equation for the probability distribution of a bacterium. Therefore, we will simulate at the microscopic model level and use coarse integration (section 4) to evolve that distribution.

3.1.1. Signal transduction. A minimal model representing the signal transduction process includes fast excitation and slow adaptation to an external stimulus and is given in [27]:

$$(3.1) \qquad \frac{du_1}{dt} = \frac{(f(S) - u_2) - u_1}{\tau_e},$$

$$(3.2) \qquad \frac{du_2}{dt} = \frac{f(S) - u_2}{\tau_a},$$

where τ_e and τ_a are the excitation and adaptation times, respectively, with $\tau_e \ll \tau_a$. We identify u_1 with the deviation of [CheY-P] from its steady state value and u_2 as the number of methylated receptors per unit volume. $f(S) = f(S(\vec{r}))$ is a function of the external stimulus; for example, it could be the number of bound receptors per unit volume in the presence of an external signal concentration, S:

$$(3.3) \qquad f = N_T S/(K_L + S).$$

N_T is the total number of receptors per unit volume, and K_L is the dissociation constant for the ligand-binding process.

The formal solution to the internal signal transduction variables $(u_1(t), u_2(t))$ for each cell can be obtained by integrating (3.1)–(3.2) in time. However, because $S(\vec{r}) = S(\vec{r}(t))$, where $\vec{r}(t)$ is a vector of random variables that represents the cell's position at time t in a given external concentration field, the integration takes place along the cell trajectory, which is a biased random walk: $\vec{r}(t')$ for $t' < t$ biases the probability of $\vec{r}(t)$. Hence, $S(\vec{r}(t))$ is a function of the unknown position, and the integration must be carried out computationally. In this work, we restrict our attention to chemotaxis in one spatial direction, x.

3.1.2. Motor and cell response. We adopt a stochastic approach to modeling the response of the flagellar motor to the regulator species, CheY-P. The motor is assumed to be in thermal equilibrium between two states, CW or CCW, corresponding to clockwise or counterclockwise rotation [28, 29]. The rates of transition between these states are functions of [CheY-P]:

$$(3.4) \qquad CCW_i \underset{k_-}{\overset{k_+}{\rightleftarrows}} CW_i, \quad i = 1, \ldots, N_f,$$
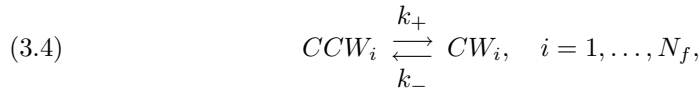
where N_f is the number of flagella per cell. For any concentration of CheY-P, the motor has a nonzero probability of being in either state. Given the state of the flagellum at time t, the probability of waiting at least a time T for a transition from CCW to CW, Φ_+, or a transition from CW to CCW, Φ_-, is given by

$$(3.5) \qquad \Phi_\pm = e^{-\int_t^{t+T} k_\pm(t')dt'}.$$

In this work, we use equilibrium transition rates, $k_\pm$, consistent with recent experimental measurements [25] of the single flagellum CW bias, b_{CW}, and the reversal frequency, w, as functions of [CheY-P]. The rates are related to these measured quantities according to [30, 31]

$$(3.6) \qquad b_{CW} = \frac{k_+}{k_+ + k_-},$$

$$(3.7) \qquad w = \frac{2 k_+ k_-}{k_+ + k_-},$$

where the reversal frequency is the harmonic mean of the transition rates. We take b_{CW} to be described by a Hill function, $b_{CW} = y_p{}^h / (K_M{}^h + y_p{}^h)$, where $y_p = $[CheY-P], with experimentally measured values for the Hill coefficient and dissociation constant, equal to $h = 10.3$ and $K_M = 3.1\,\mu\text{M}$ [25]. In these experiments, it was noted that fits to the data were consistent with $w = (2\,\mu\text{M}\,s^{-1})\,db_{CW}/dy_p$. Based on this observation [25], the transition rates as a function of [CheY-P] are

$$(3.8) \qquad k_+ = \frac{h\,y_p{}^{h-1}}{K_M{}^h + y_p{}^h},$$

$$(3.9) \qquad k_- = \frac{1}{y_p} \frac{h\,K_M{}^h}{K_M{}^h + y_p{}^h}.$$

In a constant chemoattractant field, [32, 18] show that the "voting hypothesis" is successful in producing the correct running bias of the cell from the individual flagellar bias. Although cooperativity among the flagella is not yet fully understood, we similarly adopt the "majority rules" algorithm to determine whether each cell will run or tumble in the presence of a chemoattractant gradient by constructing

$$(3.10) \qquad \nu(t) = \sum_{i=1}^{N_f} s^{(i)}(t),$$

where $s^{(i)}(t) = 0, 1$ is the state of the ith flagellum at time t, corresponding to CW and CCW directions of rotation, respectively. If $N_f/2$ or more flagella are determined to be in the CCW state, the cell in our model runs; otherwise, it tumbles. Cells run at a constant speed, v_{cell}; a cell that runs coming out of a tumble randomly selects its direction of motion to be left or right with equal probability.

3.1.3. Combining signal transduction with motor and cell response. Although we use a toy excitation-adaptation model to describe signal transduction, it is coupled with an experimentally realistic description of the flagellar switch. To do so requires introducing (i) a shift in the steady state value of u_1 and (ii) an amplification or gain factor,[1] g_0, for the signal transduction network, required so that the output of this toy model of the network spans the dynamic range of the motor:

$$(3.11) \qquad y_p = \bar{y}_p - g_0\,u_1.$$

---

[1] The issue of gain in chemotaxis continues to receive much attention [33, 34, 35]. Given the level of simplicity of our signal transduction model, we do not imply this treatment of network gain to be physically realistic. An obvious drawback is that, like other parameters in the toy model (excitation and adaptation times), it is static, whereas in the actual biological system, these parameters depend on the external signal.

Parameter	Value
τ_a	100 s
τ_e	0.1 s
g_0	5
N_T	$15\,\mu\mathrm{M}$
K_L	$1\,\mu\mathrm{M}$
$\bar{y}_p$	$2.95\,\mu\mathrm{M}$
K_M	$3.1\,\mu\mathrm{M}$
v_{cell}	$20\,\mu\mathrm{m\,s}^{-1}$
N_f	6

Hence, in section 3.2, the transition rates between the two states of a flagellum are obtained as $k_\pm(t) = k_\pm(y_p(t))$, with y_p given above. These rates are governed by (3.1)–(3.2) (together with (3.8)–(3.9) and (3.11)) and depend on the history of the cell's biased random walk trajectory in the chemoattractant field, $S(x(t))$. The flagellar states at a given time, represented by $\nu(t)$, depend on these rates through (3.5) and ultimately determine the cell's motion.

In Table 1, we report the numerical values for the model parameters that operationally interface the toy signal transduction model with the realistic model of the flagellar switch, as well as other physical constants. Although the choice of toy model parameters are "physically motivated," we do not attempt to make direct correspondence with experimental values.

3.2. Monte Carlo scheme. Below, we present a Monte Carlo scheme for implementing the microscopic model of bacterial chemotaxis described in section 3.1. For each cell at the discrete time t_n, we describe how to update the discrete flagellar states (according to (3.5)), the cell's position (according to (3.10) and subsequent discussion), and the signal transduction variables (according to (3.1)–(3.2)):

(a) Each flagellum has a state $\mathrm{s}_n^{(i)}$, where $\mathrm{s}_n^{(i)} = 0$ if CW_i and $\mathrm{s}_n^{(i)} = 1$ if CCW_i. To determine $\mathrm{s}_{n+1}^{(i)}$, for each flagellum we draw a uniformly distributed random number, $\zeta \in [0, 1]$.

(b) We determine an approximation to the probability for changing direction of rotation from (3.5). If the motor is probed at a time $t + T \equiv t + \Delta t$, such that $k_\pm(t)\Delta t \ll 1$, then the probability that a change in direction will have occurred in $(t, t + \Delta t)$ can be approximated as

$$(3.12) \qquad\qquad 1 - \Phi_\pm \approx k_\pm(t)\Delta t.$$

If the values of $k_\pm(t_n)$ at this time step are such that this approximation is not valid, Δt is reduced until it is. Systematic studies have been undertaken that show simulation results are qualitatively independent of the choice of Δt once the above restrictions are met. At each time step, the probability that a flagellum will change its direction of rotation is a function of [CheY-P] at that time, which depends on the trajectory that the cell has taken along the external chemoattractant gradient.

– If the flagellum is in the CW state ($\mathrm{s}_n^{(i)} = 0$) and $\zeta > k_-(t_n)\,\Delta t$, it continues in the CW state ($\mathrm{s}_{n+1}^{(i)} = 0$); else, it switches to the CCW state ($\mathrm{s}_{n+1}^{(i)} = 1$).

– If the flagellum is in the CCW state ($\mathrm{s}_n^{(i)} = 1$) and $\zeta > k_+(t_n)\,\Delta t$, it continues in the CCW state ($\mathrm{s}_{n+1}^{(i)} = 1$); else, it switches to the CW state ($\mathrm{s}_{n+1}^{(i)} = 0$).

(c) If three or more flagella are now in the CCW state, $\nu_{n+1} \geq 3$ in (3.10), and the cell runs; else, it tumbles. If the cell is determined to run and $\nu_n < 3$, the direction of motion is chosen to be left or right with equal probability. Otherwise, it continues to run in the same direction.

(d) The position of the cell, x_n, is accordingly updated to x_{n+1} (using the accepted time step Δt), with the cell speed, v_{cell}, assumed to be constant and independent of position.

(e) The signal transduction variables (u_1, u_2) are integrated in time using the forward Euler scheme. Their time history is a function of each cell's trajectory.

4. Coarse integration. For the present problem of simulating the chemotactic response of a population of independent bacteria, the microscopic phase space is a direct product of the phase space for each cell, consisting of its

- signal transduction variables: $\vec{u} = (u_1, u_2)$,
- flagellar state: $\vec{s}$, where $s^{(i)} = 0, 1$ for $i = 1 \ldots N_f$,
- position: x,
- direction of motion, $d = R, L, T$, corresponding to running right, running

left, and tumbling, respectively.

Rather than evolving all microscopic degrees of freedom, a coarse integration scheme identifies suitable reduced variable(s) to be integrated. One appropriate reduced variable in population studies is the spatial density distribution of cell positions, $\mu_0(x, t)$, obtained from the set of individual cell positions, x_j, which are a subset of the full microscopic phase space. However, it is possible that the unknown equations of the coarse description use additional variables, for example the densities of the right-moving, left-moving, and tumbling cells, ρ_i, where $i = R, L,$ or T. In this case, $\mu_0(x, t) = \sum_i \rho_i(x, t)$. Indeed, an optimal reduced representation balances accuracy and efficiency of modeling the physical process. Here, we propose to retain only the spatial density distribution $\mu_0(x, t)$ as the relevant macroscopic variable in coarse modeling of chemotaxis since, as we will demonstrate numerically, the density of cells in each state rapidly approaches a functional of the total density.

A systematic approach to testing the adequacy of a particular coarse description is discussed in [9]. It is based on locating the same fixed point at different levels of coarse description and examining the slow eigenvalues and corresponding eigenvectors of the linearization of the coarse time-stepper at these fixed points (see also the discussion in [7]).

The separation of characteristic time scales describing the underlying macroscopic and microscopic dynamics—for example, the (long) time scale on which the spatial density distribution of a population of bacteria moving in a chemoattractant profile changes versus the (short) mean runtime of a single cell—allows taking time steps in evolving the macroscopic state that are "long" in comparison with the "fast" microscopic time scales in the problem, resulting in a computationally efficient time evolution of the macroscopic state. We demonstrate this separation of time scales explicitly in section 5. Figure 1 shows a sketch of the *coarse integration* (CI) procedure, where the solid trajectories denote the *restriction* of the full dynamics onto a suitable low-dimensional subspace (see section 4.1 for how a low-dimensional representation of the macroscopic spatial distribution, $\mu_0(x, t)$, is constructed). At each CI step, the coarse-integrated solution is *lifted* from the lower-dimensional space into the full microscopic state space and evolved according to the Monte Carlo scheme, allowing the error incurred during the coarse time step to relax to the slow manifold parameterized by the cell density. Because the internal state $\{\vec{u}, \vec{s}\}$ of cells and their directions of
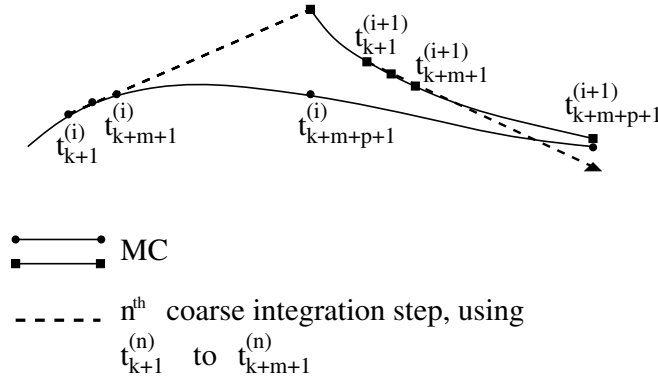
FIG. 1. *Schematic illustration of the coarse integration procedure.*

motion, d, are ignored in obtaining $\mu_0(x, t)$, they must be suitably reinitialized to construct the initial condition for the next Monte Carlo step (see section 4.2).

4.1. SVD-based restriction scheme. Below, we outline our coarse integration scheme, which operates on data from SVD of the distribution of cell positions from Monte Carlo time evolution results. In the following, the solution at a "reporting step" refers to the sorted cell positions at specified time intervals, T_{step}. Note that this time interval should be distinguished from a single Monte Carlo iteration, of which it contains a large number.

1. The Monte Carlo description is simulated for k reporting steps, corresponding to a total time interval defined as T_{settle}. Step-by-step results are accumulated for further m reporting steps, corresponding to a total time interval equal to T_{fit}, where $m = T_{fit}/T_{step}$.

2. At each reporting step, we sort the cell positions, $x_i(j)$, to obtain $X_i(j)$, $i = k+1, \ldots, k+m$, and $j = 1, \ldots, N_{\text{cells}}$. The matrix A is constructed (columnwise): $A = \{\vec{X}_{k+1}, \vec{X}_{k+2}, \ldots, \vec{X}_{k+m}\}$. Figures 2 and 3 show the chemoattractant profile and representative time sequences of sorted cell positions and corresponding histograms of the spatial density distributions, respectively. However, we find it more convenient to work with the cumulative probability distribution function, defined as

$$(4.1) \qquad P(X, t) = \frac{1}{L} \int_{x_{\min}}^{X} \mu_0(x', t) dx',$$

which is related to the sorted cell positions at that time according to

$$(4.2) \qquad j/N_{cells} = P(X_i(j), t_i),$$

where $L \equiv x_{\max} - x_{\min}$ is the spatial domain. We will use approximations to $P(X, t)$ or, equivalently, the sorted cell positions, $\vec{X}_i$, as the macroscopic variable [36].

3. Coefficients of a low-dimensional representation of the sorted cell positions are constructed in terms of orthonormal numerical basis vectors, $\{\vec{u}^{(r)}\}$, $r = 1, \ldots, r_{\max}$, where $r_{\max} \ll m$:

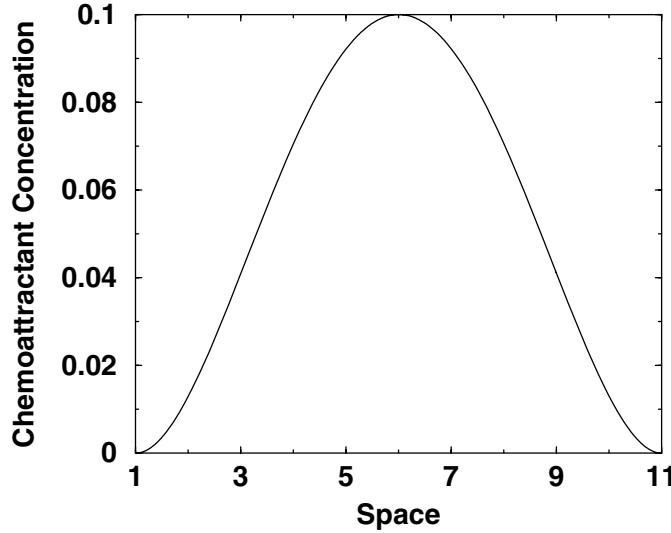$$(4.3) \qquad \alpha^{(r)}(t_i) = \vec{u}^{(r)} \cdot \vec{X}_i = \sum_{j=1}^{N_{cells}} u^{(r)}(j) X_i(j).$$

FIG. 2. *Chemoattractant profile used in Monte Carlo simulation of chemotaxis:* $S(x) = S_0(x - x_{\min})^2(x - x_{\max})^2$, *where* $S_0 = 1.6 \times 10^{-4}$ *and* $(x_{\min}, x_{\max}) = (1, 11)$. *The choice of this profile ensures zero gradient of chemoattractant at the boundaries, consistent with no-flux boundary conditions for the motion of bacteria.*

The basis vectors are obtained from SVD of the Monte Carlo data as described below.

We distinguish between two approaches to obtaining the numerical basis set.

• *Local basis vectors:* Local (in time) basis vectors are generated dynamically from m snapshots of the Monte Carlo evolution data immediately preceding each coarse integration step. The SVD of $A \equiv A_{local}$, constructed as in step 2, is computed:

$$(4.4) \qquad A_{local} = U_\ell W_\ell V_\ell^\top.$$

The columns of U_ℓ, given by $\{\vec{u_\ell}^{(r)}\}$, $r = 1, \ldots, m$, are the *local* numerical basis vectors. We assume that they remain valid basis vectors during the projective step. W_ℓ is a diagonal matrix, where $\{w_{\ell 1}, w_{\ell 2}, \ldots, w_{\ell m}\}$ are the singular values.

• *Global basis vectors:* Using a separate Monte Carlo evolution from initial conditions to steady state, T_s, the matrix $A \equiv A_{global}$ is constructed from the full data according to step 2: $A_{global} = \{\vec{X}_1, \vec{X}_2, \ldots, \vec{X}_M\}$, where $M = T_s/T_{step}$. SVD of A_{global} gives the *global* numerical basis vectors, $\{\vec{u_g}^{(r)}\}$.

We emphasize that the subscripts g and ℓ refer to the use of *global* or *local* basis vectors in the projective integration steps, respectively. Global basis vectors are computed using data from a single Monte Carlo evolution from initial conditions to steady state, while local basis vectors are computed using data from short intervals of the Monte Carlo evolution preceding each projective integration step.

4. We perform linear least squares extrapolation of $\{\alpha_{g,\ell}^{(r)}(t_i)\}$ using $i = k + 1, \ldots, k + m$ to obtain $\{\alpha_{g,\ell}^{(r)}(t_{k+m+p})\}$, corresponding to a projected time equal to T_{proj}. The projected solution is given by

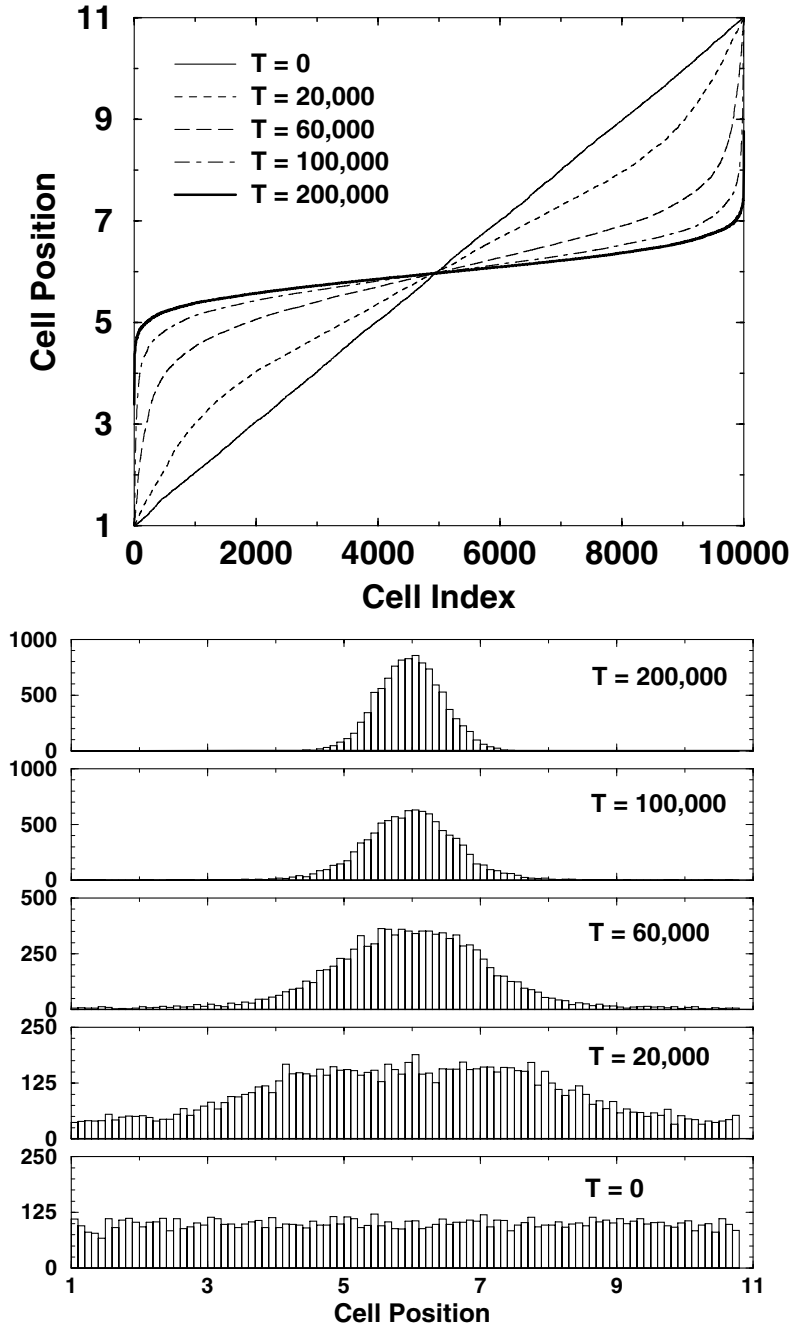$$(4.5) \qquad \vec{Y}_{k+m+p} = \sum_r \alpha_{g,\ell}^{(r)}(t_{k+m+p})\vec{u}_{g,\ell}^{(r)}.$$

FIG. 3. *Sorted cell positions (top) and corresponding histograms (bottom) using a bin size equal to* 0.1 *at* $T = 0$ *(thin solid line),* $T = 20,000$ *(dashed line),* $T = 60,000$ *(long-dashed line),* $T = 100,000$ *(dot-dashed line), and* $T = 200,000$ *(thick solid line). From the time evolution of the variance of these distributions we have determined that at* $T = 200,000$ *the coarse solution is very close to the stationary state.*

5. In practice, we use only the numerical basis vectors associated with the dominant singular values, $r = 1, \ldots, r_{\max}$, where the truncated number of basis vectors, $r_{\max}$, depends on the spectrum of singular values (in general, $r_{\max} \ll m \ll M$).

Note that at each coarse integration step, initial data from $t = t_n$ to $t = t_n + T_{settle}$ are not used in computing the numerical basis vectors (when using a *local* basis set) or the linear least squares extrapolation of the coefficients of the low-dimensional basis set. This Monte Carlo simulation interval allows for relaxation of the numerical error associated with reinitialization of the internal degrees of freedom of each cell following the $(n-1)$th coarse integration step (see section 4.2).

The use of empirical orthogonal eigenvectors, also referred to as the Karhunen–Loève expansion or the proper orthogonal decomposition, obtained through SVD of experimental or simulation data for model reduction, originates with Lorenz in the context of weather prediction [37] and has found widespread use in the dynamical systems context since the mid-1980's (see the monograph [38] and references therein).

The SVD process is computationally expensive, so if the computational cost of the microscopic cell simulations were small, using global basis vectors generated in a preliminary run would be less costly than using local basis vectors. However, in a simulation of a large number of cells, the total microscopic simulation cost for the cell population may be much larger than that for the SVD process. For example, in the numerical experiments reported here the CPU time for one simulation step of an individual cell was 2.07 microseconds, while the time for one SVD step was 22.4 milliseconds. However, in a simulation of 10^4 cells using local basis vectors, the microscopic integration routine was called 4×10^9 times versus 16 calls on the SVD routine so that 0.0041% of the time was spent on SVD.

4.2. Reinitialization of internal variables. A consistent scheme for combining microscopic and macroscropic descriptions of a physical process is central to multiscale modeling. Here, to alternate each CI step with Monte Carlo, in principle allowing relaxation of the numerical error in the projective step, we must define an appropriate reinitialization procedure: We know the position of each cell, x, after the CI step, but we discard all information about its internal state, $\{\vec{u}, \vec{s}\}$, given by the values of the signal transduction variables and the flagellar states, and its direction of motion, d_j.

Our reinitialization protocol is empirically motivated: the signal transduction variables are set equal to their local equilibrium values, $\vec{u}_j = \{0, f(S(x_j))\}$, where j refers to the jth cell. This allows the subsequent response of each cell to be within the most sensitive range of the motor gain. For simplicity, all (six) flagella are restarted in the CW state, $\vec{s}_j = \{0, 0, \ldots, 0\}$. In Figure 4, we show relaxation of the ratios of the numbers of right, left, and tumbling cells at a set location along the chemoattractant profile. These ratios at steady state for a flat chemoattractant profile are

$$(4.6) \qquad \frac{\rho_R + \rho_L}{\mu_0} = B,$$

where the right- and left-moving ratios are equal. For the present choice of numerical parameters, $B \sim 0.86$ and $\rho_R = \rho_L \sim 0.43$. Other flagellar reinitialization schemes lead to similarly rapid relaxation rates.

5. Numerical results.

5.1. Low-dimensional representation. In Figures 5 and 6, we show the first four dominant global basis vectors and singular values obtained from Monte Carlo
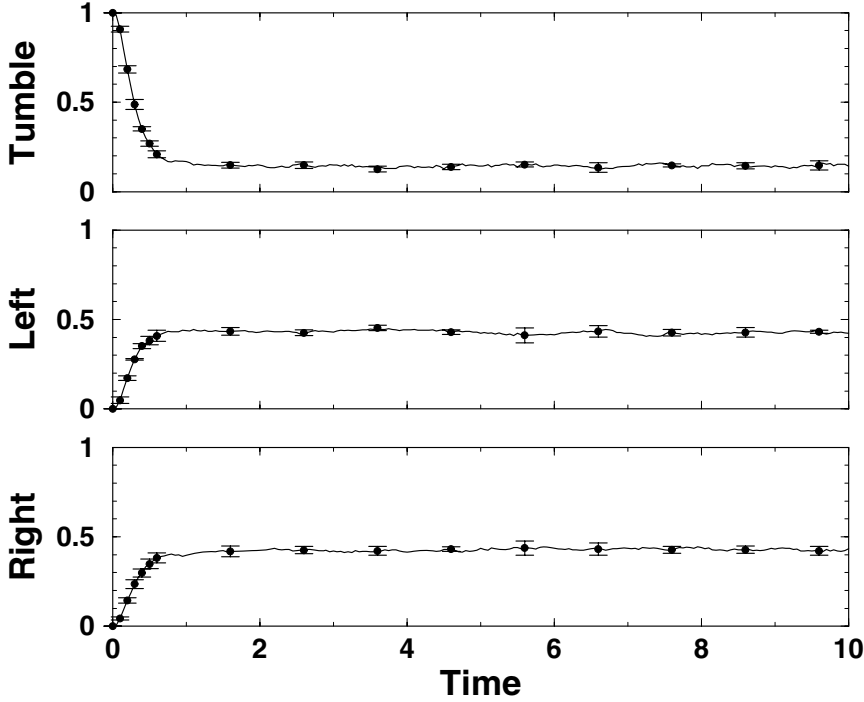
FIG. 4.   *Ratios of right-moving, left-moving, and tumbling cells at $x = 4(\pm 0.1)$ using $j = 1, \ldots, N_{cells} = 100,000$ and starting from an initially uniform distribution of cells along the chemoattractant profile: Averages over five Monte Carlo realizations started from different random number seeds are plotted. The error bars, corresponding to the root-mean-square of the distribution of these ratios, are shown for select points. We note fast relaxation of these ratios to their equilibrium values. The signal transduction variables were initialized to their local equilibrium values, $\vec{u}_j = \{0, f(S(x_j))\}$.*

evolution of $N_{cells} = 10^4$ from initial conditions to steady state. Figure 7 shows the mean coefficients over $N_{\mathrm{MC}} = 10$ Monte Carlo realizations,

$$(5.1) \qquad \bar{\alpha}^{(r)}(t) = \frac{1}{N_{\mathrm{MC}}} \sum_{k=1}^{N_{\mathrm{MC}}} \alpha_g^{(r)}(t; k),$$

and the root-mean-square of the distribution of coefficients, given by

$$(5.2) \qquad \sigma_\alpha^{(r)}(t) = \left\{ \frac{1}{N_{\mathrm{MC}} - 1} \sum_{k=1}^{N_{\mathrm{MC}}} [\alpha_g^{(r)}(t; k) - \bar{\alpha}^{(r)}(t)]^2 \right\}^{1/2}.$$

Hence, the error bars in this figure denote the expected statistical variation in the values of these coefficients as a function of time.

In Figure 8, we show the low-dimensional representation of the coarse-integrated solution for $T_{settle} = T_{fit} = 5 \times 10^2$ and $T_{proj} = 5 \times 10^3$. For each CI step, after evolving the Monte Carlo for T_{settle}, we use a linear fit to $\{\alpha_g^{(1)}(t), \alpha_g^{(2)}(t), \alpha_g^{(3)}(t), \alpha_g^{(4)}(t)\}$ during the interval T_{fit} to project the solution forward in time by T_{proj}. The points correspond to averages over $N_{\mathrm{MC}} = 5$ realizations, and the error bars give the root-mean-square of the distribution of these coefficients. For reference, we have included
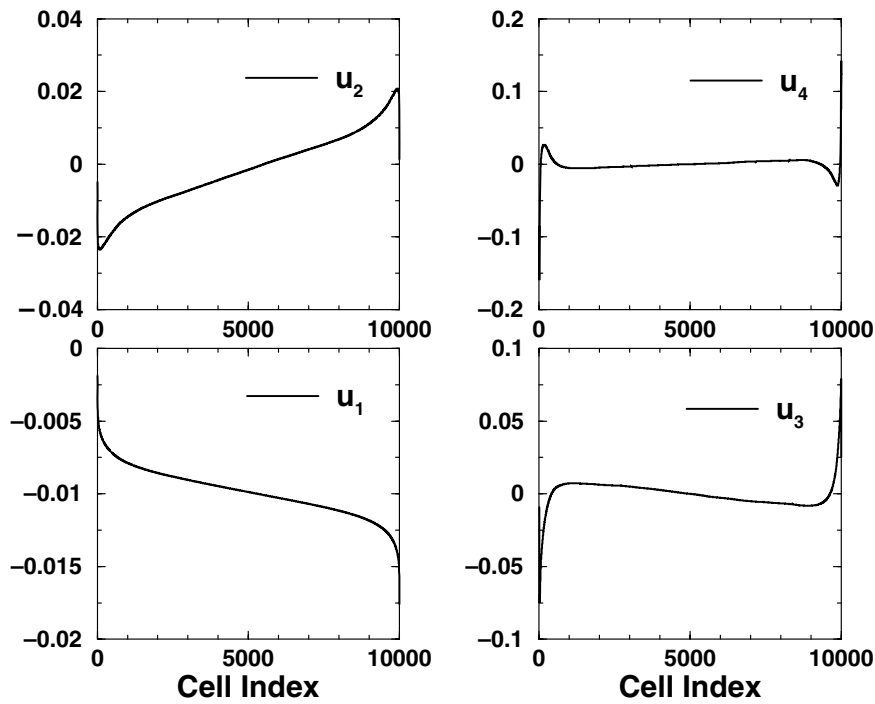
FIG. 5. $\{\vec{u}_g^{(r)}\}$, $r = 1, \ldots, 4$, are the first four global SVD basis vectors for the cumulative cell density.
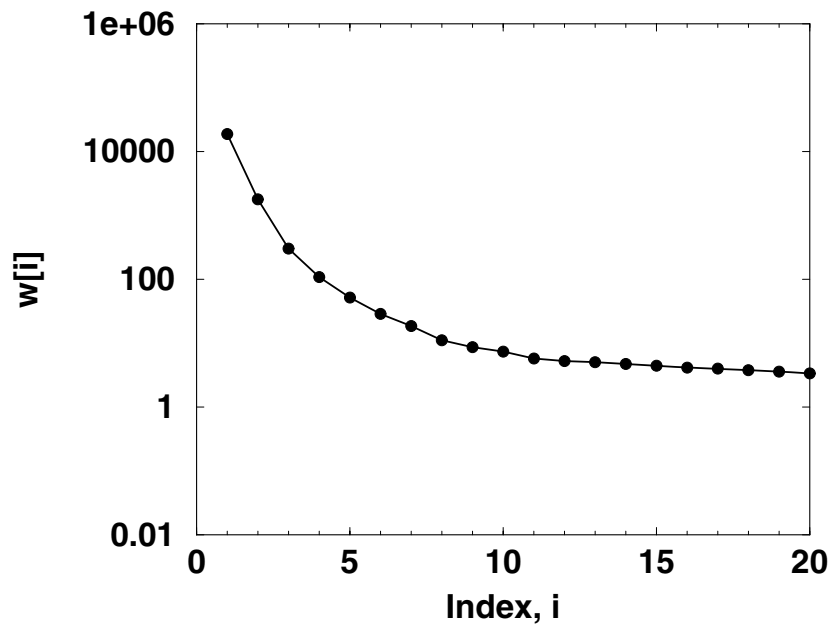

FIG. 6. Largest singular values from global SVD of Monte Carlo data from initial conditions to steady state ($T_s = 200,000, T_{step} = 200$). The first four dominant modes ($r_{max} = 4$) are used to construct the low-dimensional representation of the cumulative cell density distribution.
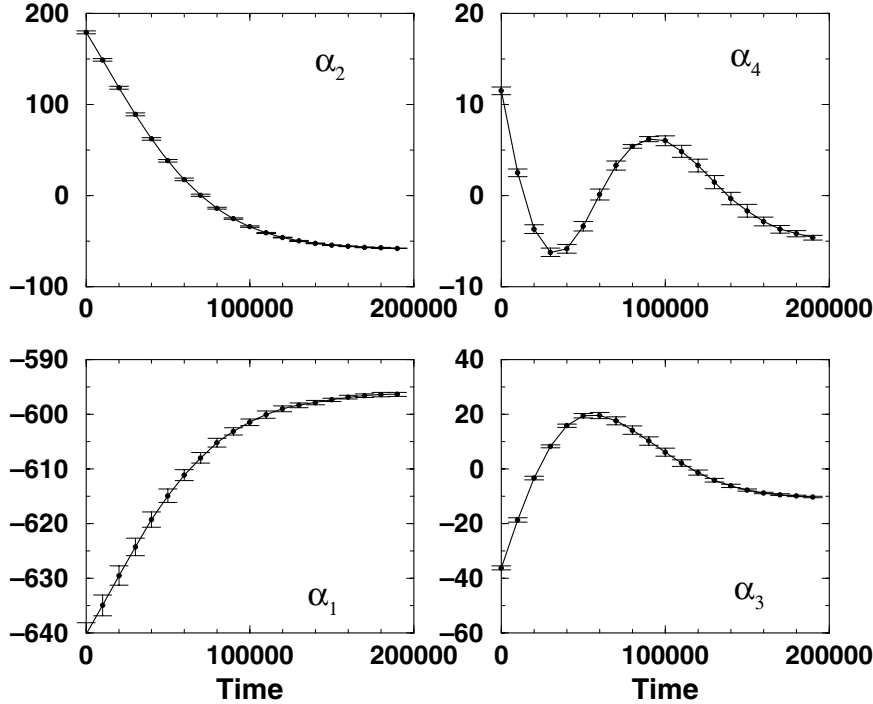
FIG. 7. *Coefficients of SVD basis vectors:* $\alpha_g^{(r)}(t_i) = \vec{u}_g^{(r)} \cdot \vec{X}_i = \sum_{j=1}^{N_{cells}} u_g^{(r)}(j) X_i(j)$, *where the points represent averages over* $N_{MC} = 10$ *Monte Carlo realizations, starting from different random number seeds. The global basis vectors* $\{\vec{u}_g^{(r)}\}$ *are obtained from one of the Monte Carlo runs. The error bars, plotted for select points, correspond to the root-mean-square of the distribution of coefficients.*

the average Monte Carlo coefficients in this figure. These results indicate that for the higher order coefficients, $\{\alpha_g^{(3)}(t), \alpha_g^{(4)}(t)\}$, whose coarse dynamics are described by a shorter characteristic time scale, a higher order time integration scheme would be more effective than the explicit Euler method used here [39]. Consequently, although for intermediate times the agreement between the CI and Monte Carlo results exceeds the variance in the Monte Carlo evolution, our results demonstrate the relative success of a straightforward CI scheme in capturing the macroscopic dynamics of the solution.

These results also illustrate the implicit assumption of separation of time scales: The coefficients $\{\alpha_g^{(r)}(t)\}$, governing the macroscopic behavior of the system, vary on a time scale of $\mathcal{O}(10^4)$ units, while the longest microscopic time scale (adaptation time of the signal transduction model) is $\mathcal{O}(10^2)$.

5.2. Analysis of errors. For comparison of solutions at different values of the CI parameters $(T_{settle}, T_{fit}, T_{proj})$, with the Monte Carlo, we construct the following measure of relative error:

$$(5.3) \qquad \varepsilon(t) = \left\{ \frac{\sum_{r=1}^{4} \left[\alpha^{(r)}(t) - \bar{\alpha}^{(r)}(t)\right]^2}{\sum_{r=1}^{4} \left[\bar{\alpha}^{(r)}(t)\right]^2} \right\}^{1/2} .$$
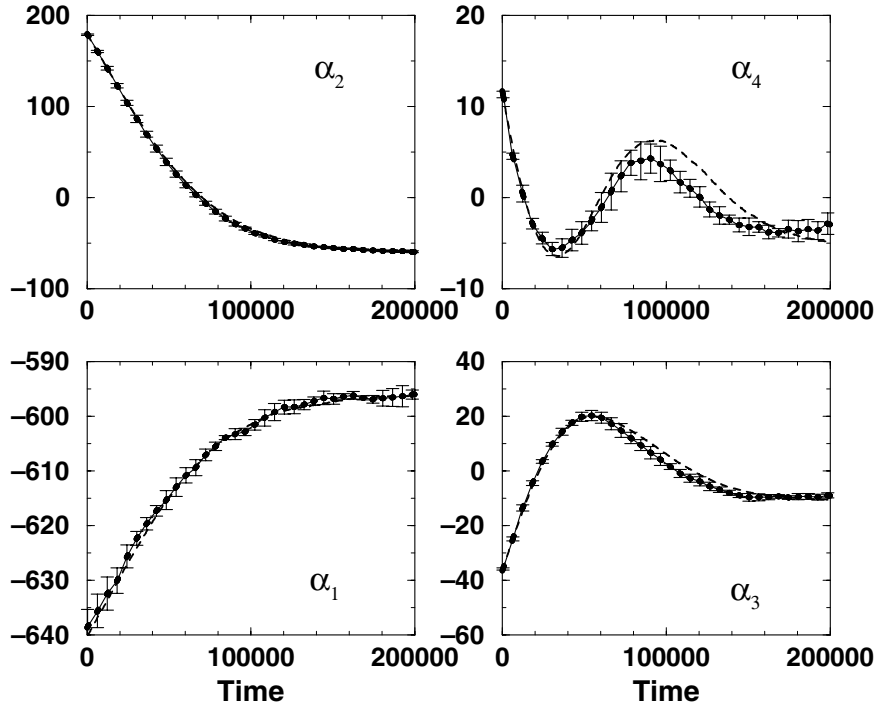
FIG. 8. *Coefficients of SVD basis vectors:* $\alpha_g^{(r)}(t_i) = \vec{u}_g^{(r)} \cdot \vec{X}_i = \sum_{j=1}^{N_{cells}} u_g^{(r)}(j) X_i(j)$, *with CI parameters* $(T_{settle}, T_{fit}, T_{proj}) = 10^3 \times (\frac{1}{2}, \frac{1}{2}, 5)$. *The points represent averages over* $N_{MC} = 5$ *realizations, starting from different random number seeds. The error bars, plotted for select points, correspond to the root-mean-square of the distribution of coefficients. The average Monte Carlo coefficients (dashed line) are shown for comparison.*

The coefficients $\{\alpha^{(r)}(t)\}, r = 1, \dots, 4$, used in computing the relative error of the CI solution are obtained as inner products of the solution with the first four basis vectors of the *global* basis set, regardless of (a) whether global or local basis vectors were used in the restricting/lifting step (hence, the subscript g is not used in (5.3) to avoid confusion with the use of local versus global basis vectors in the projective integration steps of a given CI solution) and (b) the dimensionality of the restricted space.

In Figure 9, we first plot the average relative error for $N_{MC} = 10$ Monte Carlo runs, given by

$$(5.4) \qquad \bar{\varepsilon}(t) = \frac{1}{N_{MC}} \sum_{k=1}^{N_{MC}} \varepsilon_k(t).$$

The error bars denote the error on the mean, given by $\sigma_{\bar{\varepsilon}} = \sigma_\varepsilon / \sqrt{N_{MC}}$, where σ_ε is the root-mean-square of the distribution of the error

$$(5.5) \qquad \sigma_\varepsilon(t) = \left\{ \frac{1}{N_{MC} - 1} \sum_{k=1}^{N_{MC}} [\varepsilon_k(t) - \bar{\varepsilon}(t)]^2 \right\}^{1/2}.$$

We similarly compute the relative error for CI solutions, obtained using either (i) global or (ii) local SVD basis vectors in each step. Figure 10 shows the mean errors
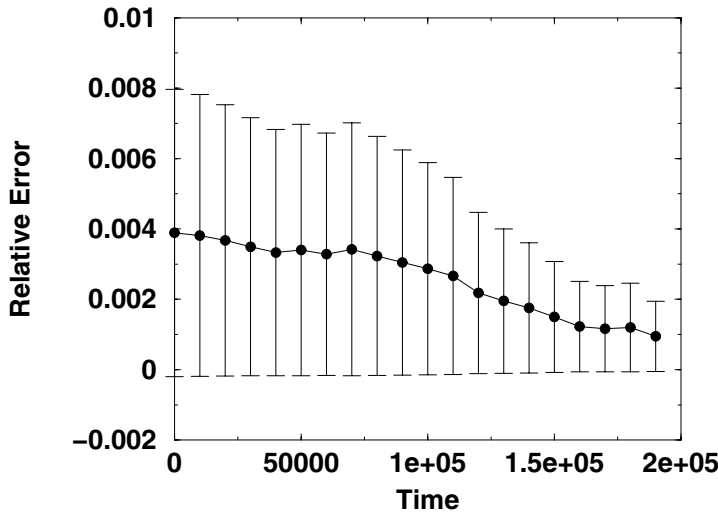
FIG. 9. *Relative error given by* $\varepsilon(t) = \{\sum_{r=1}^{4}[\alpha^{(r)}(t) - \bar{\alpha}^{(r)}(t)]^2 / \sum_{r=1}^{4}[\bar{\alpha}^{(r)}(t)]^2\}^{1/2}$: *The points correspond to the average error, obtained over* $k = 1, \ldots, 10$ *Monte Carlo realizations starting from different random number seeds. The error bars denote the error on the mean,* $\sigma_{\bar{\varepsilon}}$.
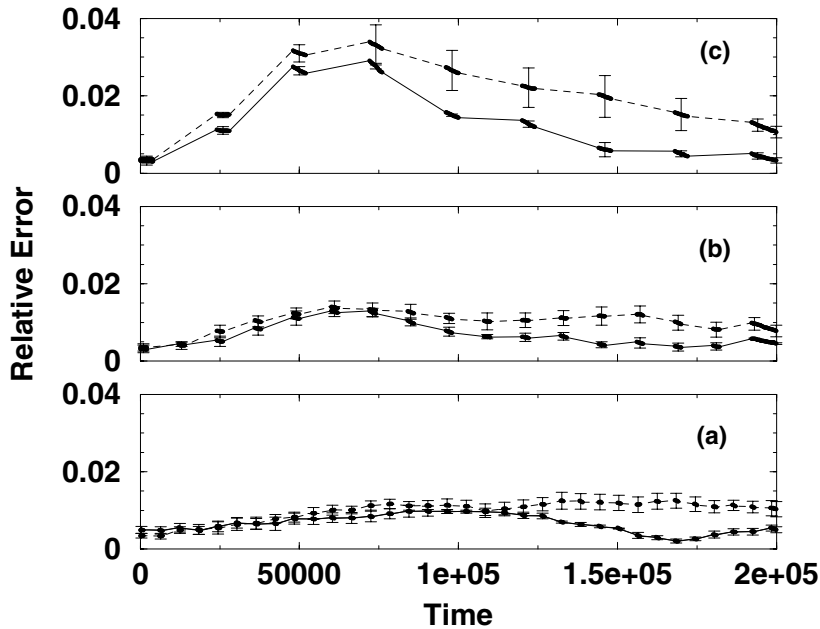

FIG. 10. *Relative error given by* $\varepsilon(t) = \{\sum_{r=1}^{4}[\alpha^{(r)}(t) - \bar{\alpha}^{(r)}(t)]^2 / \sum_{r=1}^{4}[\bar{\alpha}^{(r)}(t)]^2\}^{1/2}$, *where* $\alpha^{(r)}(t)$ *are the coefficients of the global SVD basis vectors for CI solutions corresponding to parameters* $(T_{settle}, T_{fit}, T_{proj}) = 10^3 \times (\frac{1}{2}, \frac{1}{2}, 5)$ *(bottom),* $(10^3, 10^3, 10^4)$ *(middle), and* $10^3 \times (2, 2, 20)$ *(top). The CI solution at each step was constructed using the first four global basis vectors, shown with solid lines, and using the first two local basis vectors, shown with dashed lines. The points correspond to averages over* $N_{\mathrm{MC}} = 5$ *realizations starting from different random number seeds. The error bars denote the error on the mean,* $\sigma_{\bar{\varepsilon}}$.
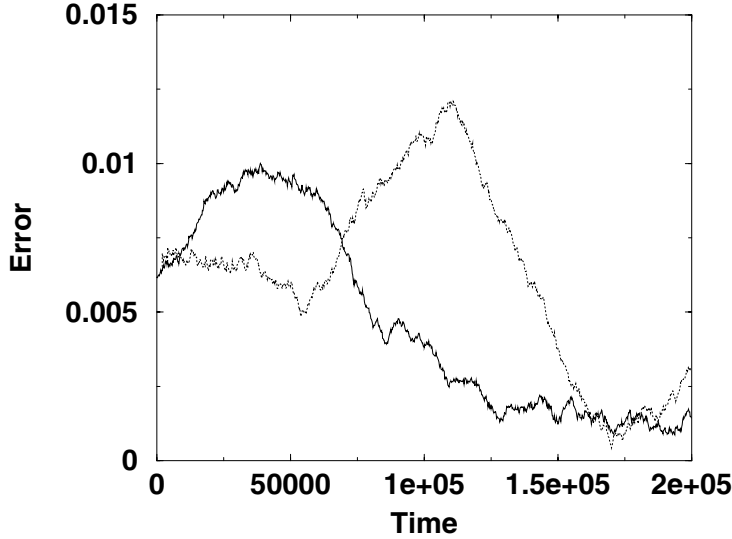
FIG. 11. *Relative error given by* $\varepsilon(t) = \{\sum_{r=1}^{4}[\alpha^{(r)}(t) - \bar{\alpha}^{(r)}(t)]^2 / \sum_{r=1}^{4}[\bar{\alpha}^{(r)}(t)]^2\}^{1/2}$ *with* $(T_{settle}, T_{fit}, T_{proj}) = 10^3 \times (1,1,0)$ *(no projective integration): After each* $(T_{settle} + T_{fit})$ *interval, the Monte Carlo evolution is restarted from its low-dimensional representation given by* $\{\alpha_g^{(1)}, \ldots, \alpha_g^{(4)}\}$ *(dotted line) or* $\{\alpha_g^{(1)}, \ldots, \alpha_g^{(8)}\}$ *(solid line).*

for solutions with CI parameters given by $(T_{settle}, T_{fit}, T_{proj}) = 10^3 \times (\frac{1}{2}, \frac{1}{2}, 5), 10^3 \times (1,1,10)$ and $10^3 \times (2,2,20)$. Note that for these parameter values, the "efficiency" of the CI scheme, defined as $T_{proj}/(T_{settle} + T_{fit})$, remains the same. In this figure, solid lines show results obtained using global SVD basis vectors, $\{\vec{u}_g^{(1)}, \vec{u}_g^{(2)}, \vec{u}_g^{(3)}, \vec{u}_g^{(4)}\}$, in the CI steps. Dashed lines show these results obtained using local SVD basis vectors. In the latter case, since SVD is applied to a short segment of the Monte Carlo, we found the higher order local basis vectors to be relatively "noisy"; hence, $\{\vec{u}_l^{(1)}, \vec{u}_l^{(2)}\}$ were used in each CI step. Note that the root-mean-square of the distribution of errors obtained for CI solutions using local basis vector is larger; in this case, the basis vectors themselves are also subject to statistical variations. We find that the relative errors using global SVD basis vectors are generally smaller than those corresponding to CI solutions obtained using local SVD basis vectors. Using either global or local basis vectors in the CI step, the smallest relative error is achieved with the first two sets CI of parameters, corresponding to projected time intervals short enough to resolve the macroscopic dynamics of the higher order coefficients of the low-dimensional representation of the solution.

As a benchmark, in Figure 11 we show the error obtained for $(T_{settle}, T_{fit}, T_{proj}) = 10^3 \times (1,1,0)$ using global SVD vectors $\{\vec{u}_g^{(r)}\}$, with $r = 1, \ldots, 4$ (dotted line) and $r = 1, \ldots, 8$ (solid line). These results show the error incurred in restricting the spatial distribution of cell positions to the low-dimensional representation given by $\{\alpha_g^{(r)}\}$, without the contribution from the projective step. First, we note that the maximum error obtained from the restriction to $\{\alpha_g^{(1)}, \ldots, \alpha_g^{(4)}\}$ is comparable to that from $\{\alpha_g^{(1)}, \ldots, \alpha_g^{(8)}\}$, indicating that using a higher dimensional restriction is not significantly advantageous here. Second, this error is comparable to the total error in Figure 10(b), which includes projective integration. Given that the total error
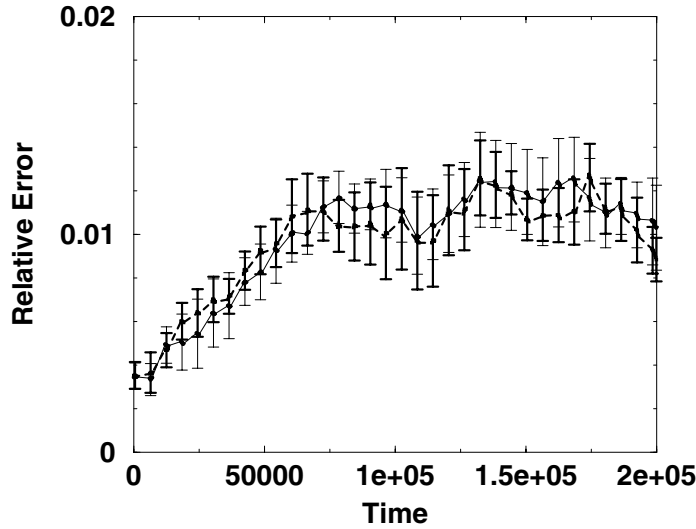
FIG. 12. *Comparison of relative errors for CI solutions (using local SVD basis vectors) corresponding to two different flagellar reinitialization schemes. The signal transduction variables were initialized to their local equilibrium values, $\vec{u}_j = \{0, f(S(x_j))\}$. In one case, all flagella were started in the CW state, shown in the thin solid line; in the second case, all flagella were started in the CCW state, with those cells to the left (right) of the chemoattractant peak running right (left), shown in the thick dashed line. The points correspond to averages over $N_{\mathrm{MC}} = 5$ realizations starting from different random number seeds. The error bars denote the error on the mean, $\sigma_{\bar{\varepsilon}}$.*

increases with a longer projective time step, T_{proj}, as shown in Figure 10(c), these results point out that the "optimal" T_{proj}, for which the errors due to the projective time step and restriction are separately comparable, is achieved in Figure 10(b).

Finally, in Figure 12, we compare CI errors using two different reinitialization schemes and find them to be equivalent.

6. Concluding remarks. We have demonstrated, through a coarse projective integration algorithm, that short bursts of appropriately initialized microscopic simulations can be used to simulate the macroscopic evolution of the cell density distribution in bacterial chemotaxis. The outer level of our computational structure was a traditional, continuum Euler integration scheme; the time derivatives of the cell density field it employed, however, were estimated from short time evolution intervals of the Monte Carlo description of this process and not evaluated from a known, macroscopic expression. This approach leads to a general framework for the computer-assisted analysis of systems whose dynamics are given at a microscopic/stochastic "fine" level but for which we require averaged, macroscopic information.

It is interesting to discuss the benefits and shortcomings of such a procedure. If accurate closed chemotactic equations exist, one should use them instead of the two-tier modeling we propose here. In addition to the insight gained from exact or approximate analytical solutions, computer-aided time evolution or bifurcation analysis using explicit equations is more efficient than kinetic Monte Carlo simulations. However, if such model equations are not available, our hybrid computational approach can become more economical than long time direct Monte Carlo simulation. Furthermore, when one is interested in qualitative transitions or bifurcations of the macroscopic behavior, marginally stable or unstable stationary states may be difficult

to identify through direct microscopic simulations, while coarse time-stepping holds promise when combined with traditional bifurcation algorithms [7, 9, 39].

It appears, therefore, that a modeler would ultimately gain in obtaining quantitative computational answers efficiently but perhaps lose in the fundamental understanding of a physical process that macroscopic model equations would offer. Therefore a promising research direction is to use such algorithms to test the validity of explicit closures that assume slaving of certain higher order moments of the evolving distribution to lower order ones. In the chemotaxis context, when signal transduction and corresponding motor response of the cell to an external signal are taken into account as we do here, macroscopic model equations derived systematically from the microscopic description do not exist. The assumption implicit in our coarse integration algorithm was that the macroscopic description closes at the level of the spatial density distribution. In one spatial direction, for example, it would be interesting to learn when this assumption breaks down, requiring separate evolution of right-moving, left-moving, and tumbling cell density distributions.

More generally, we believe that the approach illustrated here for coarse time integration of a Monte Carlo description of bacterial chemotaxis is broadly applicable to different types of microscopic simulators describing, for example, Brownian, Lattice–Boltzmann, or molecular dynamics and leading to emergent macroscopic dynamic behavior. Such a hybrid scheme allows efficient simulation of the macroscopic behavior and may provide insight into macroscopic model equations.

REFERENCES

[1] V. B. Shenoy, R. Miller, E. B. Tadmor, D. Rodney, R. Phillips, and M. Ortiz, *An adaptive finite element approach to atomic-scale mechanics—The quasicontinuum method*, J. Mech. Phys. Solids, 47 (1999), pp. 611–642.

[2] A. L. Garcia, J. B. Bell, W. Y. Crutchfield, and B. J. Alder, *Adaptive mesh and algorithm refinement using direct simulation Monte Carlo*, J. Comput. Phys., 154 (1999), pp. 134–155.

[3] I. G. Kevrekidis, C. W. Gear, J. M. Hyman, P. G. Kevrekidis, O. Runborg, and K. Theodoropoulos, *Equation-free multiscale computation: Enabling microscopic simulators to perform system-level tasks*, Commun. Math. Sci., 1 (2003), pp. 715–762.

[4] K. Theodoropoulos, Y. H. Qian, and I. G. Kevrekidis, *"Coarse" stability and bifurcation analysis using timesteppers: A reaction diffusion example*, Proc. Natl. Acad. Sci. USA, 97 (2000), pp. 9840–9843.

[5] C. W. Gear, I. G. Kevrekidis, and C. Theodoropoulos, *"Coarse" integration/bifurcation analysis via microscopic simulators: Micro-Galerkin methods*, Comp. Chem. Engrg., 26 (2002), pp. 941–963.

[6] J. Li, P. G. Kevrekidis, C. W. Gear, and I. G. Kevrekidis, *Deciding the nature of the coarse equation through microscopic simulations: The baby-bathwater scheme*, Multiscale Model. Simul., 1 (2003), pp. 391–407.

[7] A. G. Makeev, D. Maroudas, and I. G. Kevrekidis, *"Coarse" stability and bifurcation analysis using stochastic simulators: Kinetic Monte Carlo examples*, J. Chem. Phys., 116 (2002), pp. 10083–10091.

[8] A. G. Makeev, D. Maroudas, A. Z. Panagiotopoulos, and I. G. Kevrekidis, *Coarse bifurcation analysis of kinetic Monte Carlo simulations: A lattice gas model with lateral interactions*, J. Chem. Phys., 117 (2002), pp. 8229–8240.

[9] C. Siettos, M. D. Graham, and I. G. Kevrekidis, *Coarse Brownian dynamics for nematic liquid crystals: Bifurcation, projective integration and control via stochastic simulation*, J. Chem. Phys., 118 (2003), pp. 10149–10157.

[10] G. Hummer and I. G. Kevrekidis, *Coarse molecular dynamics of a peptide fragment: Free energy, kinetics and long time dynamics computations*, J. Chem. Phys., 118 (2003), pp. 10762–10773.

[11] M. Melchior and H. C. Oettinger, *Variance reduced simulations of stochastic differential equations*, J. Chem. Phys., 103 (1995), pp. 9506–9509.

[12] M. MELCHIOR AND H. C. OETTINGER, *Variance reduced simulations of polymer dynamics*, J. Chem. Phys., 105 (1996), pp. 3316–3331.

[13] H. G. OTHMER AND T. HILLEN, *The diffusion limit of transport equations V: Chemotaxis equations*, SIAM J. Appl. Math., 62 (2002), pp. 1222–1250.

[14] R. ERBAN AND H. G. OTHMER, *From individual to collective behavior in bacterial chemotaxis*, SIAM J. Appl. Math., 65 (2004), pp. 361–391.

[15] R. ERBAN AND H. G. OTHMER, *From signal transduction to spatial pattern formation in* E. coli: *A paradigm for multiscale modeling in biology*, Multiscale Model. Simul., 3 (2005), pp. 362–394.

[16] R. M. MACNAB AND D. E. KOSHLAND, *The gradient-sensing mechanism in bacterial chemotaxis*, Proc. Natl. Acad. Sci. USA, 69 (1972), pp. 2509–2512.

[17] S. M. BLOCK, J. E. SEGALL, AND H. C. BERG, *Adaptation kinetics in bacterial chemotaxis*, J. Bacteriol., 154 (1983), pp. 312–323.

[18] J. E. SEGALL, S. M. BLOCK, AND H. C. BERG, *Temporal comparisons in bacterial chemotaxis*, Proc. Natl. Acad. Sci. USA, 83 (1986), pp. 8987–8991.

[19] J. B. STOCK AND M. G. SURETTE, *Chemotaxis*, in Escherichia coli and Salmonella: Cellular and Molecular Biology, F. C. Neidhardt, ed., ASM Press, Washington, D.C., 1996, pp. 1103–1129.

[20] J. STOCK AND S. DA RE, Encyclopedia of Microbiology, 1 (2000), pp. 772–780.

[21] N. BARKAI AND S. LEIBLER, *Robustness in simple biochemical networks*, Nature, 387 (1997), pp. 913–917.

[22] P. A. SPIRO, J. S. PARKINSON, AND H. G. OTHMER, *A model of excitation and adaptation in bacterial chemotaxis*, Proc. Natl. Acad. Sci. USA, 94 (1997), pp. 7263–7268.

[23] C. J. MORTON-FIRTH AND D. BRAY, *Predicting temporal fluctuations in an intracellular signalling pathway*, J. Theoret. Biol., 192 (1998), pp. 117–128.

[24] H. C. BERG AND E. M. PURCELL, *Physics of chemoreception*, Biophys. J., 20 (1977), pp. 193–219.

[25] P. CLUZEL, M. SURETTE, AND S. LEIBLER, *An ultrasensitive bacterial motor revealed by monitoring signaling proteins in single cells*, Science, 287 (2000), pp. 1652–1655.

[26] M. J. KIM, J. C. BIRD, A. J. VAN PARYS, K. S. BREUER, AND T. R. POWERS, *A macroscopic scale model of bacterial flagellar bundling*, Proc. Natl. Acad. Sci. USA, 100 (2003), pp. 15481–15485.

[27] H. G. OTHMER AND P. SCHAAP, *Oscillatory cAMP signaling in the development of Dictyostelium discoideum*, Comments Theor. Biol., 5 (1998), pp. 175–282.

[28] S. M. BLOCK, J. E. SEGALL, AND H. C. BERG, *Adaptation kinetics in bacterial chemotactis*, J. Bacteriol., 154 (1983), pp. 312–323.

[29] R. M. MACNAB, *Flagellar switch*, in Two-Component Signal Transduction, J. A. Hock and T. J. Silhavy, eds., ASM, Washington, D.C., 1995, pp. 181–199.

[30] B. E. SCHARF, K. A. FAHRNER, L. TURNER, AND H. C. BERG, *Control of direction of Flagellar rotation in bacterial chemotaxis*, Proc. Natl. Acad. Sci. USA, 95 (1998), pp. 201–206.

[31] L. TURNER, A. D. T. SAMUEL, A. S. STERN, AND H. C. BERG, *Temperature dependence of switching of the bacterial flagellar motor by the protein CheY($13DK106YW$)*, Biophys. J., 77 (1999), pp. 597–603.

[32] A. ISHIHARA, J. E. SEGALL, S. M. BLOCK, AND H. C. BERG, *Coordination of flagella on filamentous cells of Escherichia coli*, J. Bacteriol., 155 (1983), pp. 228–237.

[33] F. W. DAHLQUIST, *Science's STKE* (2002), http://www.stke.org/cgi/content/full/OC_sigtrans; 2002/132/pe24.

[34] D. BRAY, *Bacterial chemotaxis and the question of gain*, Proc. Natl. Acad. Sci. USA, 99 (2002), pp. 7–9.

[35] V. SOURJIK AND H. C. BERG, *Receptor sensitivity in bacterial chemotaxis*, Proc. Natl. Acad. Sci. USA, 99 (2002), pp. 123–127.

[36] C. W. GEAR, *Projective Integration Methods for Distributions*, NEC TR 2001-130, Princeton, NJ, 2001.

[37] E. N. LORENZ, *Empirical Orthogonal Functions and Statistical Weather Prediction*, Tech. rep. 1, MIT, Department of Meteorology, Statistical Forecasting Project, Cambridge, MA, 1956.

[38] P. J. HOLMES, J. L. LUMLEY, AND G. BERKOOZ, *Turbulence, Coherent Structures, Dynamical Systems and Symmetry*, Cambridge University Press, Cambridge, UK, 1996.

[39] R. RICO-MARTINEZ, C. W. GEAR, AND I. G. KEVREKIDIS, *Coarse projective kMC integration: Forward/reverse initial and boundary value problems*, J. Comput. Phys., 196 (2004), pp. 474–489.